Inorganic Chemistry

Article

pubs.acs.org/IC

Performance Improvement of Lithium Manganese Phosphate by Controllable Morphology Tailoring with Acid-Engaged Nano Engineering

Hui Guo,[†] Chunyang Wu,[†,‡] Longhuan Liao,[†] Jian Xie,*[,†,‡] Shichao Zhang,[§] Peiyi Zhu,[∥] Gaoshao Cao,*[,‡] and Xinbing Zhao[†,‡]

[†]State Key Laboratory of Silicon Materials, Department of Materials Science and Engineering, Zhejiang University, Hangzhou 310027, China

[‡]Key Laboratory of Advanced Materials and Applications for Batteries of Zhejiang Province, Hangzhou 310027, China

[§]School of Materials Science and Engineering, Beijing University of Aeronautics and Astronautics, Beijing 100191, China

[∥]Industrial Technology Research Institute of Zhejiang University, Hangzhou 310058, China

Supporting Information

ABSTRACT: Olivine-type lithium manganese phosphate ($LiMnPO_4$) has been considered as a promising cathode for next-generation Li-ion batteries. Preparation of high-performance $LiMnPO_4$ still remains a great challenge because of its intrinsically low Li-ion/electronic conductivity. In this work, significant performance enhancement of $LiMnPO_4$ has been realized by a controllable acid-engaged morphology tailoring from large spindles into small plates. We find that acidity plays a critical role in altering the morphology of the $LiMnPO_4$ crystals. We also find that size decrease and plate-like morphology are beneficial for the performance improvement of $LiMnPO_4$. Among the plate-like samples, the one with the smallest size shows the best electrochemical performance. After carbon coating, it can deliver high discharge capacities of 104.0 mAh g^{-1} at 10 C and 85.0 mAh g^{-1} at 20 C. After 200 cycles at 1 C, it can still maintain a high discharge capacity of 106.4 mAh g^{-1}, showing attractive applications in high-power and high-energy Li-ion batteries.

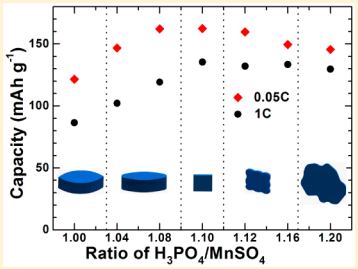

INTRODUCTION

The great energy demand for portable electronic devices has stimulated the development of advanced electrical energy storage systems. Recently, the emerging global trend to replace or reduce the use of the fossil fuels by clean energy, such as solar, wind, and hydroelectric energy has also promoted the requirement for a new generation of electrical energy storage system.[1,2] For now and the foreseeable future, Li-ion batteries remain the most promising candidates for their high theoretical energy density (both gravimetric and volumetric), portability, and durability.[3,4] It is well-known, however, that the energy density of current Li-ion batteries is limited mainly by the inherent low energy density of the available cathode materials.[1] Therefore, searching for a cathode material with high capacity and voltage has become an urgent issue both scientifically and technologically.

The olivine-type $LiMnPO_4$ offers a higher energy density than the already commercialized $LiFePO_4$, due to its higher redox potential of Mn^{2+}/Mn^{3+}(4.1 V vs Li/Li^+) compared with Fe^{2+}/Fe^{3+} (3.45 V vs Li/Li^+). The excellent thermal stability, environmental benignity, and safety make it a promising cathode material for the future battery systems.[5−9] However, the intrinsically low electronic conductivity and sluggish Li-ion diffusion rate result in poor electrochemical properties, such as low capacity, poor rate capability, and limited cycle life. Similar to $LiFePO_4$, the electronic conductivity of $LiMnPO_4$ can be enhanced by carbon coating. However, a great challenge still remains to develop high-performance $LiMnPO_4$ since Li ions diffuse through a one-dimensional channel along the *b*-axis in the olivine structure.[6]

Creating nanostructured crystals represents one of the most practical strategies to enhance the electrochemical performance of olivine-structured $LiMnPO_4$, because nanoscale materials with proper dimensions and architectures have the potential to significantly improve the transport of both electrons and Li ions.[10−12] Especially, decreasing the length along the [010] direction or enlarging the exposed (010) facet could lead to a dramatic improvement in rate performance considering the one-dimensional diffusion path of Li ions along the *b*-axis in the olivine framework.[13,14] Until now, many researchers have reported the performance enhancement of $LiMnPO_4$ by preparing nanoscale crystals.[15−19] Excellent rate capability and cycle performance have been reported in the (010) facet orientated $LiMnPO_4$ nanoplates.[20] In this regard, the electrochemical properties of $LiMnPO_4$ are largely determined by the morphology of the crystals. Besides, the fundamental research has shown that some intrinsic issues of $LiMPO_4$ (M = Fe, Mn),

Received: October 29, 2014
Published: January 5, 2015

DOI: 10.1021/ic5026075
Inorg. Chem. 2015, 54, 667−674

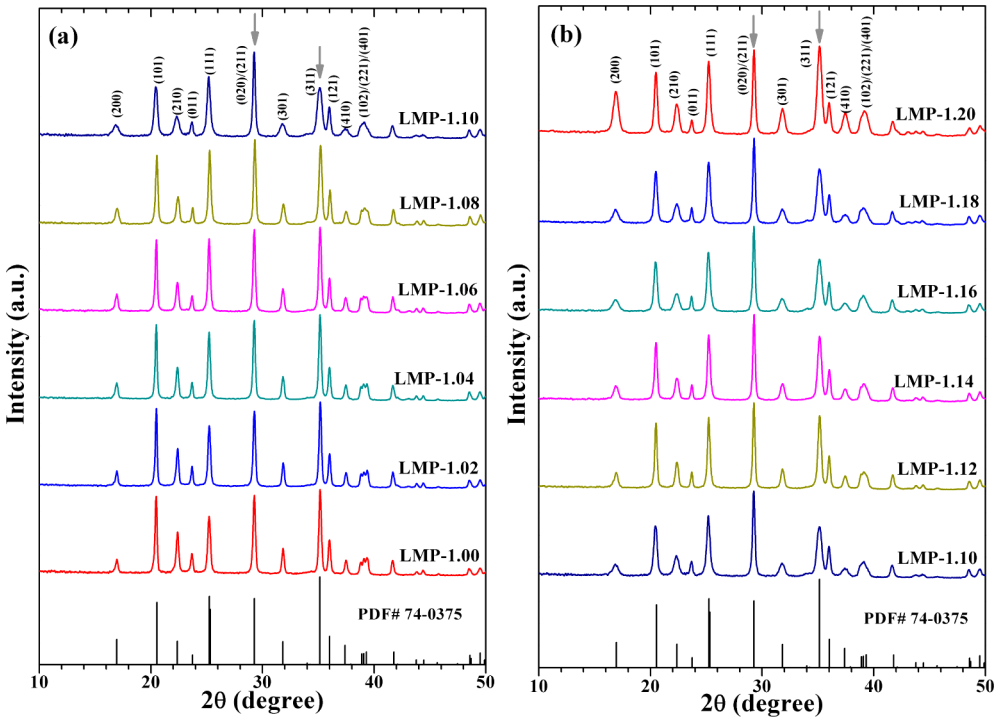

Figure 1. XRD patterns of $LiMnPO_4$ synthesized with $H_3PO_4/MnSO_4$ ratios: (a) 1.00−1.10 and (b) 1.10−1.20.

such as solubility limits, equilibrium compositions, and intercalation/deintercalation mechanisms of Li ions, also highly depend on the particle morphology.[13,21]

Hydrothermal/solvothermal reactions provide a facile approach to prepare $LiMnPO_4$ nanocrystals with varied morphologies at low temperature in comparison with other methods. The morphology could be easily tuned by either altering the synthesis conditions or selecting different raw materials, solvents and additives.[7,10,14−16,22−24] In our previous report, we found that a slight change in the ratio of the precursors could exert a great influence on the shape, size, and orientation of $LiMnPO_4$ crystals.[16] The critical role that H^+ plays in altering the crystallization habit of $LiMnPO_4$ was also found.[16] Other work also found that the crystal morphology of $LiMPO_4$ (M = Fe, Mn) was sensitive to the pH in hydrothermal/solvothermal reactions.[23,25,26]

Based on the above findings, it deserves further research to reveal the relationship between morphology evolution of $LiMnPO_4$ and acidity in the precursor by adjusting the amount of acid. This can be easily achieved since acid, for example H_3PO_4, is usually used as the precursor to synthesize $LiMnPO_4$. In this work, we made a comprehensive investigation on the morphology evolution of $LiMnPO_4$ with H_3PO_4 concentration and the related effect on the electrochemical performance. We found that the increase in H_3PO_4 proportion first results in the tailoring of large spindles of $LiMnPO_4$ into small plates with remarkably improved electrochemical performance. Further increase in H_3PO_4 proportion leads to the growth of $LiMnPO_4$ plates in the lateral direction with slightly degraded electrochemical performance. We found that $LiMnPO_4$ could exhibit excellent electrochemical performance by optimizing its morphology.

EXPERIMENTAL SECTION

Preparation of $LiMnPO_4$. Nanostructured $LiMnPO_4$ was synthesized by solvothermal route using ethylene glycol (EG) based solvent. In a typical synthesis, EG solutions of LiOH and H_3PO_4 were prepared separately by adding LiOH (0.03 mol) in 40 mL of EG and H_3PO_4 (various amounts) in 20 mL of EG. Meanwhile, the 0.01 mol $MnSO_4$ was first dissolved in 5 mL of deionized (DI) water followed by adding 35 mL of EG with stirring to form $MnSO_4$ solution. The H_3PO_4 solution was then added to the LiOH solution very slowly (less than 1 mL min^{-1}) with vigorous stirring. A white suspension formed after this mixing process. Afterward, the $MnSO_4$ solution was introduced slowly to the above white suspension. The final mixture was magnetically stirred for 10 min before it was transferred to a 120 mL Teflon-lined stainless steel autoclave. The solvothermal reaction was performed at 180 °C for 10 h. The white precipitate was collected by centrifugation, washed by DI water and absolute ethanol repeatedly, and dried at 60 °C for 12 h. The molar ratio of $H_3PO_4/MnSO_4$ in the precursor was varied from 1.00 to 1.40 and the product was named LMP-x (x is the molar ratio of $H_3PO_4/MnSO_4$). For instance, sample LMP-1.02 means the ratio of $H_3PO_4/MnSO_4/LiOH$ is 1.02:1:3 and the amount of H_3PO_4 in the precursor is 0.0102 mol.

Synthesis of $LiMnPO_4$/C Composites. For carbon coating, the solvothermal products were mixed with glucose (the mass ratio of $LiMnPO_4$/glucose is 2:1) in DI water to form dispersions. After drying, the mixture was fired under Ar atmosphere at 600 °C for 4h with a heating rate of 5 °C min^{-1}. For simplicity, the name of the carbon-coated $LiMnPO_4$ ($LiMnPO_4$/C) is same as that of the corresponding solvothermal product.

Materials Characterization. The crystal structures of the solvothermal products were checked by X-ray diffraction (XRD) on a Rigaku D/Max-2550pc powder diffractometer equipped with Cu K_α radiation (λ = 1.541 Å). Scanning electron microscopy (SEM) images were observed on an S-4800 field emission scanning electron microscope (Hitachi, Japan). Transmission electron microscopy (TEM) and high-resolution TEM (HRTEM) images were observed on a FEI Tecnai G2 F20 S-Twin high-resolution transmission electron microscope with an acceleration voltage of 200 kV. Carbon content analysis of $LiMnPO_4$/C was conducted on a Flash EA 1112 tester. This equipment allows the combustion of solid carbon into gaseous CO_2 in a rapid and dynamic mode (flash roasting). The content of carbon then can be determined by analyzing the amount of CO_2 using precise chromatographic analysis technique.

DOI: 10.1021/ic5026075
Inorg. Chem. 2015, 54, 667−674

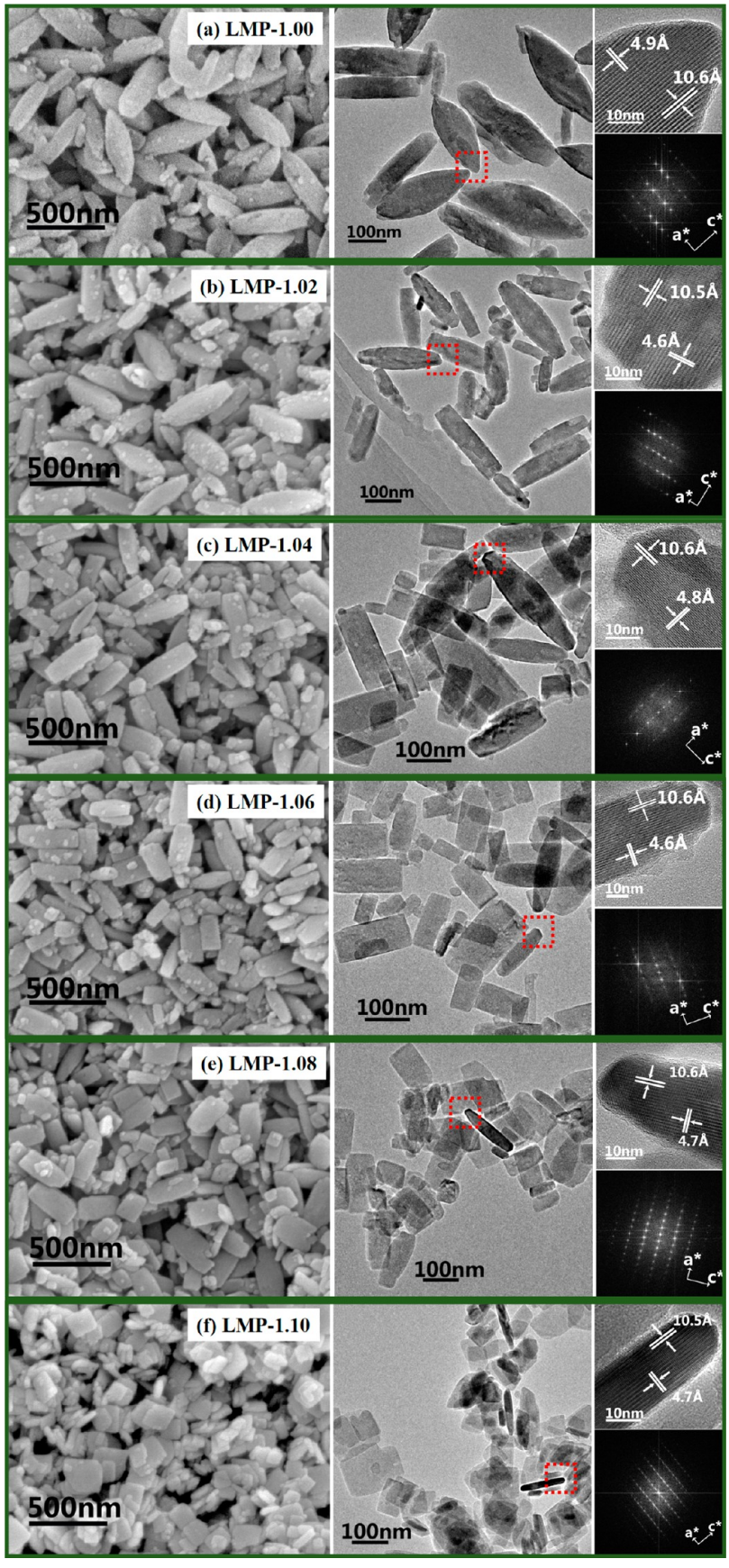

Figure 2. SEM images, TEM images, HRTEM images, and FFT patterns of $LiMnPO_4$: (a) LMP-1.00, (b) LMP-1.02, (c) LMP-1.04, (d) LMP-1.06, (e) LMP-1.08, and (f) LMP-1.10.

DOI: 10.1021/ic5026075
Inorg. Chem. 2015, 54, 667−674

Electrochemical Measurements. Electrochemical performance of $LiMnPO_4$/C was evaluated by galvanostatic cycling using CR2025-type coin cells. The electrode slurry was made by mixing 70 wt % $LiMnPO_4$/C, 20 wt % acetylene black, and 10 wt % polyvinylidene fluoride (PVDF) in *N*-methyl pyrrolidone (NMP) with magnetic stirring for 2 h. The slurry was then pasted uniformly on Al foil and dried at 100 °C under vacuum overnight to make the working electrodes. The electrodes were then assembled into half cells in an Ar-filled glovebox using Li foil as counter electrode and Celgard 2300 film as separator. The electrolyte was 1 M $LiPF_6$ dissolved in ethylene carbonate (EC)/diethyl carbonate (DEC) (1:1 in volume). The cells were tested over a voltage range of 2.0−4.5 V (vs Li/Li^+) using a constant-current−constant-voltage (CC−CV) mode on a Neware BTS-5 V-10 mA battery cycler (Shenzhen, China). The current was set based on the mass of $LiMnPO_4$ and 1C is 170 mA g^{-1}. The specific capacity was calculated based on the weight of bare $LiMnPO_4$ (excluding coated carbon). All of the electrochemical measurements were carried out at room temperature.

RESULTS AND DISCUSSION

Figure 1 shows the XRD patterns of the solvothermal products by increasing the ratio of $H_3PO_4/MnSO_4$ in the precursor from 1.00 to 1.20. All the diffraction peaks of the samples could be indexed to olivine-type $LiMnPO_4$ with a *Pnmb* space group (JCPDS card no. 74-0375) and no impurity phase is detected. It is worth noting that the relative intensity of the diffraction peaks varies with increased H_3PO_4 amount in the precursor. For LMP-1.00, the highest reflection is (311) peak, which is in agreement with the standard patterns. The strongest reflection, however, changes to (020) peak when the ratio of $H_3PO_4/MnSO_4$ increases to 1.08 as indicated by the arrows in Figure 1a. The (311) peak becomes the strongest once again for LMP-1.20 (Figure 1b). Note that, the $I_{(020)}/I_{(200)}$ intensity ratio in all of the samples is larger than 1. According to Kanamura et al.,[26] the formation of plate-like $LiMnPO_4$ with a large exposed *ac*-plane is expected if $I_{(020)} > I_{(200)}$. In our work, however, a different result is observed as discussed later.

Figure 2 shows the SEM, TEM, and HRTEM images and the fast Fourier transform (FFT) patterns of $LiMnPO_4$ with $H_3PO_4/MnSO_4$ molar radio ranging from 1.00 to 1.10. In Figure 2a, the $LiMnPO_4$ crystal exhibits a spindle-like shape with a length of ∼320 nm, a width of ∼120 nm, and a mean thickness of ∼70 nm. The interplanar spacings of ∼10.6 and ∼4.9 Å shown by the HRTEM image in Figure 2a correspond to the (100) and (001) lattice planes, respectively. HRTEM images and FFT patterns reveal that the length, width and thickness directions in the spindle-like crystal correspond to the *c*-axis, *a*-axis and *b*-axis of the $LiMnPO_4$ lattice, and that the largest exposed facet of the spindle-like crystals is the *ac*-plane. For the following characterization, the *ac*-plane is tracked to investigate the effect of the different amounts of H_3PO_4 on the crystallization behavior of $LiMnPO_4$, as marked by the red square in each figure. As shown in Figure 2b−f, with gradual increase in $H_3PO_4/MnSO_4$ ratio, the length and width of the spindle-like crystals decrease continuously, finally to 100 and 15 nm for sample LMP-1.10.

On one hand, the *ac*-plane of $LiMnPO_4$ undergoes a rapid "tailoring" process from arc shape in LMP-1.00 (Figure 2a) to rectangular shape in LMP-1.10 (Figure 2f). The thickness of crystals (*b*-axis direction), on the other hand, shows a gradual increase from 70 nm in LMP-1.00 to 100 nm in LMP-1.10. Clearly, LMP-1.10 exhibits a largest exposure of *bc*-plane, in contrast to the XRD result which predicts the largest exposed facet is the *ac*-plane. From the above results, we can see that the morphology evolution of $LiMnPO_4$ is closely related to the $H_3PO_4/MnSO_4$ ratio, and that both size and orientation of the $LiMnPO_4$ crystals can be altered by simply changing the H_3PO_4 concentration. The morphology evolution of $LiMnPO_4$ is described schematically in Figure 3.

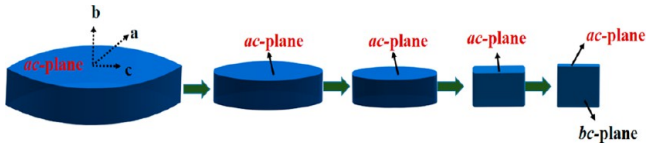

Figure 3. Schematic illustration of morphology evolution of $LiMnPO_4$ with increased $H_3PO_4/MnSO_4$ ratio (1.00−1.10) in the precursor.

The plate-like morphology keeps unchanged when increasing the ratio of $H_3PO_4/MnSO_4$ from 1.10 to 1.20, as shown in Figure 4. However, the edges of the $LiMnPO_4$ plates become irregular and the average width increases to around 300 nm in LMP-1.20 (Figure 4f). Figure 5 shows the TEM and FFT of LMP-1.20. The interplanar spacings of 3.12 and 2.48 Å in Figure 5b can be identified as the (020) and (002) lattice planes. This indicates that the largest exposed facet of the nanoplates in LMP-1.20 is the *bc*-plane, keeping the same orientation with LMP-1.10. Based on the above observations, morphology evolution of $LiMnPO_4$ with $H_3PO_4/MnSO_4$ ratio at 1.10−1.20 range is illustrated in Figure 6. Further increasing the $H_3PO_4/MnSO_4$ ratio to 1.30 and 1.40 will lead to a continuous growth of plate-like $LiMnPO_4$ in the lateral direction (Figure S1). During the synthesis, we found that a gel-like matter forms when too much H_3PO_4 (in EG) was added to LiOH (in EG) and the gel-like matter cannot dissolve $MnSO_4$. As a result, we failed to prepare the $LiMnPO_4$ when the ratio of $H_3PO_4/MnSO_4$ exceeds 1.40.

From the above analysis, the morphology evolution of $LiMnPO_4$ experiences a two-step process with increasing the $H_3PO_4/MnSO_4$ ratio. In the first step, $LiMnPO_4$ crystallizes from spindle-like shape to plate-like one as the $H_3PO_4/MnSO_4$ ratio increases from 1.00 to 1.10. In this step, the width (parallel to the *a*-axis) and length (parallel to the *c*-axis) of the crystals decrease gradually while the thickness (parallel to *b*-axis) increases slightly, with both the size and orientation changed. In the second step, the lateral size of the plate-like $LiMnPO_4$ is on the increase with increased $H_3PO_4/MnSO_4$ ratio (1.10−1.20) while the orientation of the crystals is kept unchanged. It is widely accepted that the formation of $LiMnPO_4$ can be expressed as

$$H_3PO_4 + 3LiOH + MnSO_4 = LiMnPO_4 + Li_2SO_4 + 3H_2O \quad (1)$$

when the $LiOH/H_3PO_4/MnSO_4$ ratio is 3:1:1. As we previously stated, the addition of excess H_3PO_4 in the precursor actually provides more H^+ in the solvent. The notable effect of pH on the crystal morphology and orientation was also reported in other work.[26]

To further understand the role that acidity plays in altering the crystallization habit of $LiMnPO_4$, two additional experiments were conducted where H_2SO_4 (1 mol L^{-1} aqueous solution) was added to replace the excess H_3PO_4. In one experiment, the ratio of $H_2SO_4/H_3PO_4/MnSO_4/LiOH$ is 0.075:1:1:3, where the H^+ concentration is equal to that in LMP-1.05. The product is named LMP-S1. In the other

DOI: 10.1021/ic5026075
Inorg. Chem. 2015, 54, 667−674

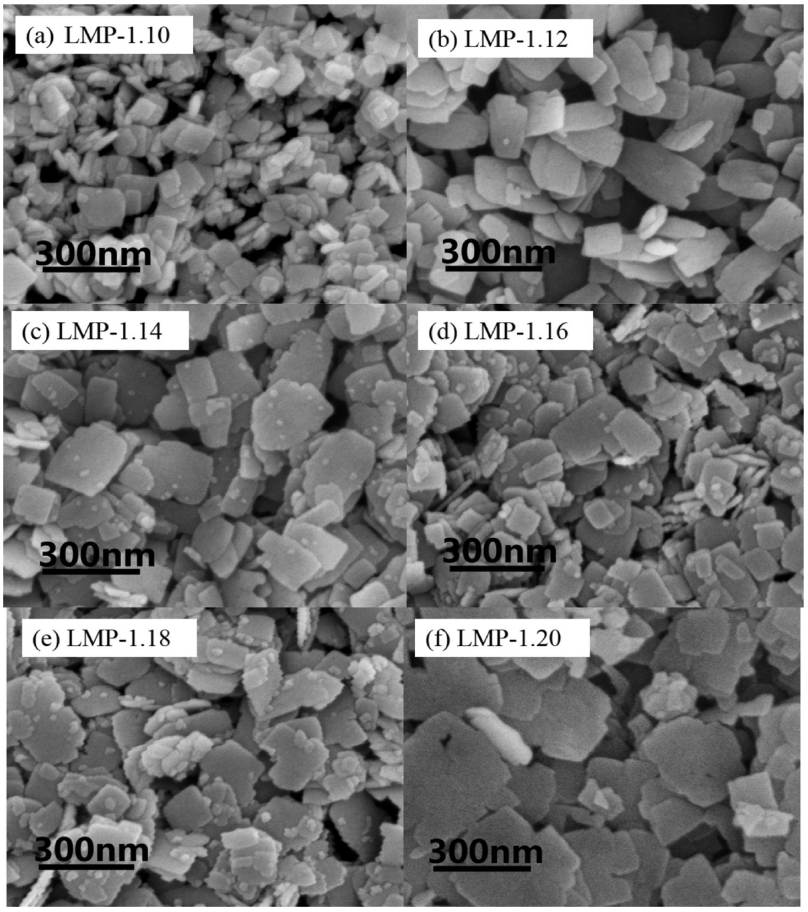

Figure 4. SEM images of $LiMnPO_4$: (a) LMP-1.10, (b) LMP-1.12, (c) LMP-1.14, (d) LMP-1.16, (e) LMP-1.18, and (f) LMP-1.20.

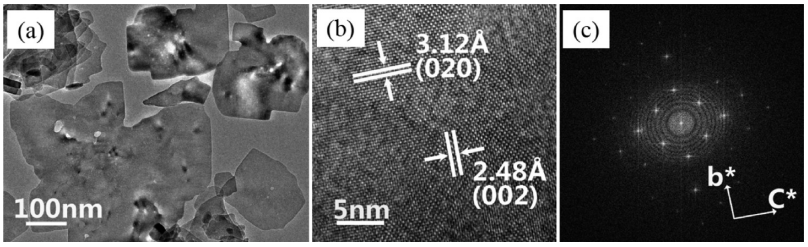

Figure 5. (a) TEM image, (b) HRTEM image, and (c) FFT patterns of LMP-1.20.

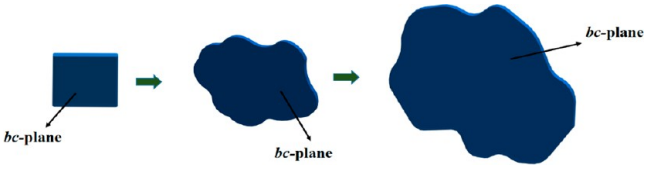

Figure 6. Schematic illustration of morphology evolution of $LiMnPO_4$ with increased $H_3PO_4/MnSO_4$ ratio (1.10−1.20) in the precursor.

experiment, the ratio of $H_2SO_4/H_3PO_4/MnSO_4/LiOH$ is 0.225:1:1:3, where the H^+ concentration is equal to that in LMP-1.15. The product is named LMP-S2. Figure 7 gives the SEM images of LMP-S1 and LMP-S2. LMP-S1 exhibits a quasi spindle-like shape with a width of ∼80 nm, a length of ∼260 nm, and an average thickness of ∼90 nm. The morphology of LMP-S1 is very familiar to those of LMP-1.04 and LMP-1.06. LMP-S2 exhibits a plate-like shape with a width of ∼150 nm, and as expected, it exhibits a similar morphology with LMP-1.14 and LMP-1.16. The results confirm that the acidity indeed plays a critical role in determining the morphology of $LiMnPO_4$ in the solvothermal reaction.

The relationship between morphology and electrochemical properties of $LiMnPO_4$ is investigated by performing cycling tests on several typical samples including LMP-1.00, LMP-1.04, LMP-1.08, LMP-1.10, LMP-1.12, LMP-1.16, and LMP-1.20. Before the electrochemical tests, carbon coating was conducted to increase the electronic conductivity. Note that these samples show a similar carbon content (Table S1) and that carbon coating does not change the morphology of the solvothermal products obviously (Figure S2). Figure 8 shows the first discharge curves of the selected samples at 0.05 C. All the samples exhibit a discharge plateau at around 4.15 V (vs Li/Li^+), related to the redox couple of Mn^{3+}/Mn^{2+} of $LiMnPO_4$ (Figure 8a). The correlation between the discharge capacity and the $H_3PO_4/MnSO_4$ ratio is plotted in Figure 8b. This correlation actually reflects the relationship between the

DOI: 10.1021/ic5026075
Inorg. Chem. 2015, 54, 667−674

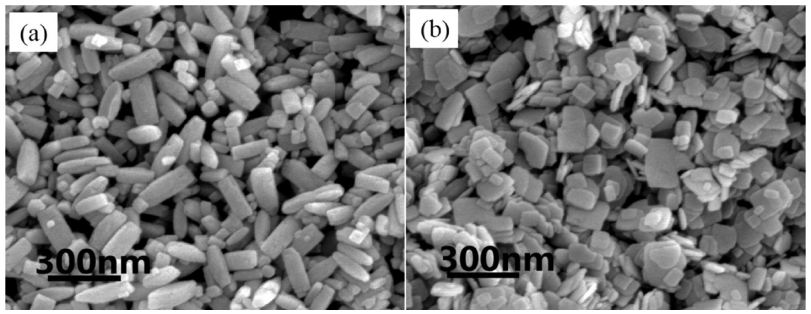

Figure 7. SEM images of (a) LMP-S1 and (b) LMP-S2.

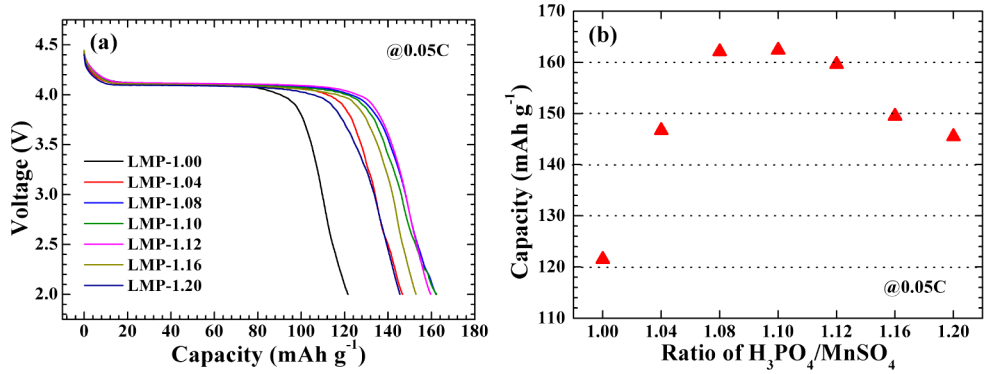

Figure 8. (a) Discharge profiles of the selected samples at 0.05 C and (b) discharge capacity at 0.05 C as a function of $H_3PO_4/MnSO_4$ ratio.

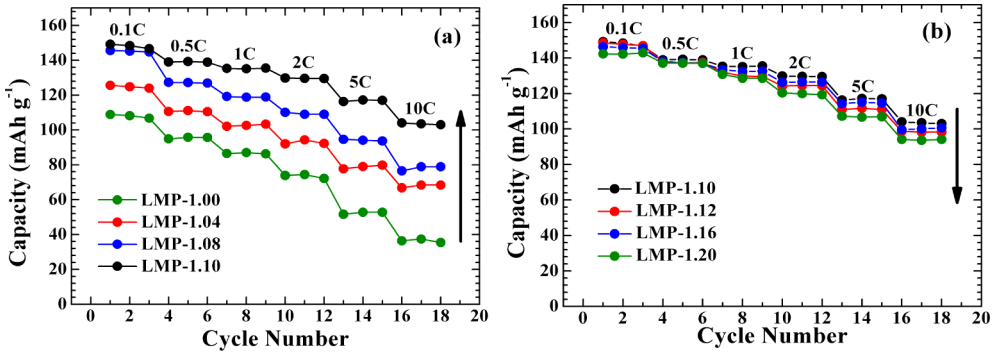

Figure 9. Comparison of rate capability of (a) LMP-1.00, LMP-1.04, LMP-1.08, and LMP-1.10 and (b) LMP-1.10, LMP-1.12, LMP-1.16, and LMP-1.20.

electrochemical performance and the crystal morphology of $LiMnPO_4$. Among these samples, LMP-1.00 exhibits the lowest capacity of only 121.5 mAh g^{-1}. The discharge capacity gets an obvious increase as the $H_3PO_4/MnSO_4$ ratio increases from 1.00 to 1.10. LMP-1.04, LMP-1.08, and LMP-1.10 deliver discharge capacities of 146.7, 162.1, and 162.4 mAh g^{-1}, respectively, reaching 86.3%, 95.3%, and 95.5% of the theoretical capacity of $LiMnPO_4$.

Even though the largest exposed facet in LMP-1.00 is the desired *ac*-plane, it shows the lowest discharge capacity. This can be attributed to its large dimension of width (parallel to *a*-axis) and length (parallel to *c*-axis) in the spindle-like shape, which restricts the charge transfer within the spindle and renders sluggish Li-ion diffusion kinetics. As the ratio of $H_3PO_4/MnSO_4$ increases, the size of $LiMnPO_4$ crystals decreases rapidly along *a*-axis and *c*-axis direction, enhancing the electrochemical kinetics and thus increasing the capacity. The increase of $H_3PO_4/MnSO_4$ ratio from 1.10 to 1.20 results in obvious lateral growth of the $LiMnPO_4$ plates, leading to increased Li-ion diffusion length along *b*-axis and thus reduced discharge capacity. Consequently, compared with LMP-1.10, LMP-1.12, LMP-1.16, and LMP-1.20 deliver lower discharge capacities of 159.6, 149.5, and 145.5 mAh g^{-1}, respectively.

Figure 9 compares rate performance of the selected samples. For the rate capability tests, the cells were charged at 0.1 C to 4.5 V, kept at 4.5 V for 1 h, and then discharged at various rates, from C/10 to 10 C. As expected, the LMP-1.00 shows the lowest discharge capacity at each applied rate. The discharge capacities at various rates increase rapidly when the ratio of $H_3PO_4/MnSO_4$ increases from 1.00 to 1.10 (Figure 9a), which can be attributed to the decreased crystal size. At 1 C, LMP-1.00, LMP-1.04, LMP-1.08, and LMP-1.10 deliver discharge capacities of 86.5, 102.1, 119.2, and 135.3 mAh g^{-1}, respectively. Clearly, the discharge capacity is sensitive to the $H_3PO_4/MnSO_4$ ratio at 1.00−1.10. For all the plate-like samples, in contrast, the discharge capacities show a slight decrease at each rate as the ratio of $H_3PO_4/MnSO_4$ increases from 1.10 to 1.20 (Figure 9b). At 10 C, LMP-1.10, LMP-1.12,

DOI: 10.1021/ic5026075
Inorg. Chem. 2015, 54, 667−674

LMP-1.16, and LMP-1.20 can still deliver high discharge capacities of 104.0, 98.7, 99.6, and 94.1 mAh g^{-1}, respectively, indicating the excellent rate capability. Among four plate-like samples, LMP-1.10 exhibits the highest discharge capacity at each rate due to its smallest lateral size. At 20 C, LMP-1.10 can yield a high discharge capacity of 85.0 mAh g^{-1} and even at 50 C, a discharge capacity of 56.7 mAh g^{-1} is still obtainable (Figure S3). It seems that the thin plate-like morphology is beneficial for enhanced electrochemical kinetics. The electrochemical performance of our samples is superior to those of previously reported ones prepared also by the hydrothermal/solvothermal method.[15,17,18,23,27−31] Figure 10 gives the comparison of the rate performance of LMP-1.10 with that of other $LiMnPO_4$ samples that represent the best ones reported so far.

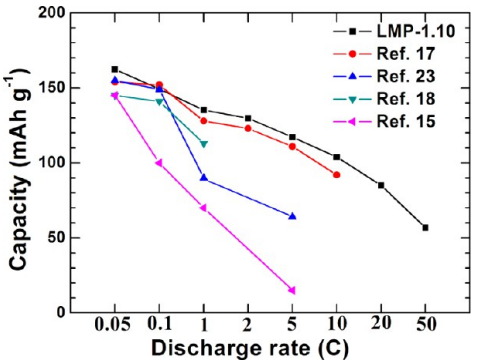

Figure 10. Comparison of rate capability of our LMP-1.10 sample with those of previously reported ones.

Figure 11 compares the cycling stability of the selected $LiMnPO_4$ samples. The cells were charged to 4.5 V at 1 C, kept at 4.5 V for 1 h, and discharged to 2.0 V at 1 C. After 200 cycles, the capacity retention is 55.9%, 74.6%, and 73.7%, respectively, for LMP-1.00, LMP-1.04, and LMP-1.08 (Figure 11a). The plate-like LMP-1.10, LMP-1.12, LMP-1.16, and LMP-1.20 exhibit a higher retention of 79.2%, 80.3%, 79.6%, and 77.6% (Figure 11b). As reported previously, the $LiMnPO_4$−$MnPO_4$ interface strain can cause a larger volume change (8.9%) than $LiFePO_4$−$FePO_4$ (7%), which accounts for relatively rapider capacity fade of $LiMnPO_4$. Our results indicate that decreasing the particle size and using the plate-like morphology may relieve the volume changes effectively, leading to excellent cycling stability of $LiMnPO_4$. Note that besides high capacity and excellent rate capability, LMP-1.10 also demonstrates superior cycling stability, maintaining a high discharge capacity of 106.4 mAh g^{-1} after 200 cycles at 1 C. The excellent electrochemical performance is ascribed to its smallest size and plate-like morphology.

CONCLUSIONS

In summary, controllable morphology tailoring of $LiMnPO_4$ nanocrystals has been realized in EG-based solvothermal reaction by simply adjusting the ratio of $H_3PO_4/MnSO_4$ from 1.00 to 1.40. The morphology evolves from spindle-like shape to plate-like one as the ratio of $H_3PO_4/MnSO_4$ increases from 1.00 to 1.10. In this process, besides the size reduction, the orientation of the crystals also experiences a gradual evolution, converting the largest exposed facet from the *ac*-plane in spindle-like $LiMnPO_4$ to the *bc*-plane in plate-like one. Further increasing the $H_3PO_4/MnSO_4$ ratio (1.10−1.40) only leads to the size increase in the *bc*-plane without orientation change. We confirm that the change in crystallization habit of $LiMnPO_4$ is sensitive to the acidity. The electrochemical performance of $LiMnPO_4$/C exhibits a close dependence on the morphology of the $LiMnPO_4$ crystals. The discharge capacity of $LiMnPO_4$/C increases as the morphology of $LiMnPO_4$ changes from lager spindles to small plates and then decreases as the plate-like crystals grow larger in lateral direction. The changes in rate capability and cycling performance exhibit a similar trend with that of the discharge capacity. Among all the samples, LMP-1.10 exhibits the highest discharge capacity, best rate capability, and also excellent cycling stability due to its plate-like shape and the smallest size.

ASSOCIATED CONTENT

Supporting Information

SEM images of LMP-1.30 and LMP-1.40, voltage profiles of LMP-1.10 at various rates, and carbon content analysis of $LiMnPO_4$/C. This material is available free of charge via the Internet at http://pubs.acs.org.

AUTHOR INFORMATION

Corresponding Authors

*Tel/Fax: +86-571-87951451. E-mail: xiejian1977@zju.edu.cn.
*E-mail: gscao@zju.edu.cn.

Notes

The authors declare no competing financial interest.

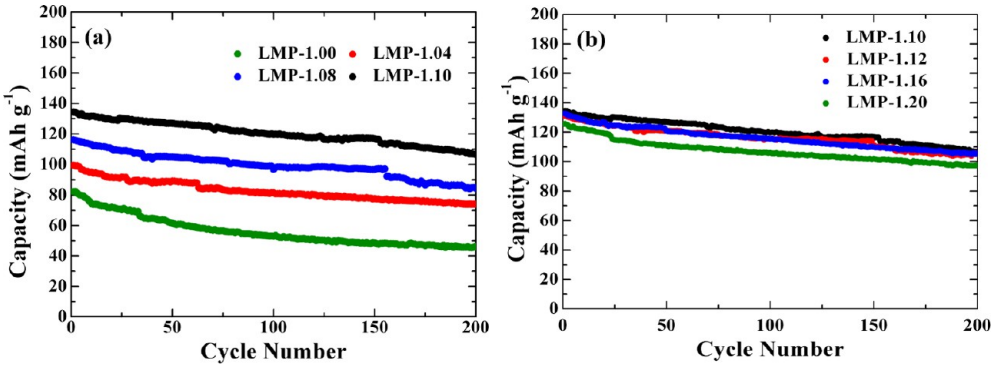

Figure 11. Comparison of cycling performance of (a) LMP-1.00, LMP-1.04, LMP-1.08, and LMP-1.10 and (b) LMP-1.10, LMP-1.12, LMP-1.16, and LMP-1.20 at 1 C.

DOI: 10.1021/ic5026075
Inorg. Chem. 2015, 54, 667−674

■ ACKNOWLEDGMENTS

This work was supported by National Basic Research Program of China (2013CB934001), the National Natural Science Foundation of China (No. 51101139), the Fundamental Research Funds for the Central Universities (2014XZZX002-03), Key Science and Technology Innovation Team of Zhejiang Province under Grant Number 2010R50013, and Program for Innovative Research Team in University of Ministry of Education of China (IRT13037).

■ REFERENCES

(1) Xu, B.; Qian, D. N.; Wang, Z. Y.; Meng, Y. S. *Mater. Sci. Eng. R.* **2012**, *73*, 51−65.
(2) Goodenough, J. B.; Kim, Y. *Chem. Mater.* **2009**, *22*, 587−603.
(3) Wang, J. J.; Li, Y. L.; Sun, X. L. *Nano Energy* **2013**, *2*, 443−467.
(4) Thackeray, M. M.; Wolverton, C.; Isaacs, E. D. *Energy Environ. Sci.* **2012**, *5*, 7854−7863.
(5) Yu, F.; Zhang, L. L.; Zhu, M. Y.; An, Y. X.; Xia, L. L.; Wang, X. G.; Dai, B. *Nano Energy* **2014**, *3*, 64−79.
(6) Aravindan, V.; Gnanaraj, J.; Lee, Y. S.; Madhavi, S. *J. Mater. Chem. A* **2013**, *1*, 3518−3539.
(7) Devaraju, M. K.; Honma, I. *Adv. Energy Mater.* **2012**, *2*, 284−297.
(8) Choi, D.; Xiao, J.; Choi, Y. J.; Hardy, J. S.; Vijayakumar, M.; Bhuvaneswari, M. S.; Liu, J.; Xu, W.; Wang, W.; Yang, Z. G.; Graff, G. L.; Zhang, J. G. *Energy Environ. Sci.* **2011**, *4*, 4560−4566.
(9) Padhi, A. K.; Nanjundaswamy, K.; Goodenough, J. B. *J. Electrochem. Soc.* **1997**, *144*, 1188−1194.
(10) Nan, C. Y.; Lu, J.; Li, L. H.; Li, L. L.; Peng, Q.; Li, Y. D. *Nano Res.* **2013**, *6*, 469−477.
(11) Mukherjee, R.; Krishnan, R.; Lu, T. M.; Koratkar, N. *Nano Energy* **2012**, *1*, 518−533.
(12) Song, M. K.; Park, S.; Alamgir, F. M.; Cho, J.; Liu, M. L. *Mater. Sci. Eng. R* **2011**, *72*, 203−252.
(13) Lu, Z. G.; Chen, H. L.; Robert, R.; Zhu, B. Y. X.; Deng, J. Q.; Wu, L. J.; Chung, C. Y.; Grey, C. P. *Chem. Mater.* **2011**, *23*, 2848−2859.
(14) Saravanan, K.; Balaya, P.; Reddy, M. V.; Chowdari, B. V. R.; Vittal, J. J. *Energy Environ. Sci.* **2010**, *3*, 457−463.
(15) Zhou, F. R.; Zhu, P. L.; Fu, X. Z.; Chen, R. Q.; Sun, R.; Wong, C. P. *CrystEngComm* **2014**, *16*, 766−774.
(16) Guo, H.; Wu, C. Y.; Xie, J.; Zhang, S. C.; Cao, G. S.; Zhao, X. B. *J. Mater. Chem. A* **2014**, *2*, 10581−10588.
(17) Dinh, H. C.; Mho, S. I.; Kang, Y. K.; Yeo, I. H. *J. Power Sources* **2013**, *244*, 189−195.
(18) Wang, D. Y.; Buqa, H.; Crouzet, M.; Deghenghi, G.; Drezen, T.; Exnar, I.; Kwon, N. H.; Miners, J. H.; Poletto, L.; Grätzel, M. *J. Power Sources* **2009**, *189*, 624−628.
(19) Martha, S. K.; Markovsky, B.; Grinblat, J.; Gofer, Y.; Haik, O.; Zinigrad, E.; Aurbach, D.; Drezen, T.; Wang, D.; Deghenghi, G. *J. Electrochem. Soc.* **2009**, *156*, A541−A552.
(20) Rui, X. H.; Zhao, X. X.; Lu, Z. Y.; Tan, H. T.; Sim, D. H.; Hng, H. H.; Yazami, R.; Lim, T. M.; Yan, Q. Y. *ACS Nano* **2013**, *7*, 5637−5646.
(21) Wagemaker, M.; Mulder, F. M.; Van der Ven, A. *Adv. Mater.* **2009**, *21*, 2703−2709.
(22) Wang, L.; He, X. M.; Sun, W. T.; Wang, J. L.; Li, Y. D.; Fan, S. S. *Nano Lett.* **2012**, *12*, 5632−5636.
(23) Qin, Z. H.; Zhou, X. F.; Xia, Y. G.; Tang, C. L.; Liu, Z. P. *J. Mater. Chem.* **2012**, *22*, 21144−21153.
(24) Nan, C. Y.; Lu, J.; Chen, C.; Peng, Q.; Li, Y. D. *J. Mater. Chem.* **2011**, *21*, 9994−9996.
(25) Qin, X.; Wang, X. H.; Xiang, H. M.; Xie, J.; Li, J. J.; Zhou, Y. C. *J. Phys. Chem. C* **2010**, *114*, 16806−16812.
(26) Dokko, K.; Koizumi, S.; Nakano, H.; Kanamura, K. *J. Mater. Chem.* **2007**, *17*, 4803−4810.
(27) Pan, X. L.; Xu, C. Y.; Hong, D.; Fang, H. T.; Zhen, L. *Electrochim. Acta* **2013**, *87*, 303−308.
(28) Cao, Y. B.; Duan, J. G.; Hu, G. R.; Jiang, F.; Peng, Z. D.; Du, K.; Guo, H. W. *Electrochim. Acta* **2013**, *98*, 183−189.
(29) Yang, S. L.; Ma, R. G.; Hu, M. J.; Xi, L. J.; Lu, Z. G.; Chung, C. Y. *J. Mater. Chem.* **2012**, *22*, 25402−25408.
(30) Choi, D.; Wang, D. H.; Bae, I. T.; Xiao, J.; Nie, Z. M.; Wang, W.; Viswanathan, V. V.; Lee, Y. J.; Zhang, J. G.; Graff, G. L. *Nano Lett.* **2012**, *10*, 2799−2805.
(31) Delacourt, C.; Poizot, P.; Morcrette, M.; Tarascon, J. M.; Masquelier, C. *Chem. Mater.* **2004**, *16*, 93−99.

DOI: 10.1021/ic5026075
Inorg. Chem. 2015, 54, 667−674